HAL
open science

A comparative study of DNS of airblast atomization using CLSMOF and CLSVOF methods

Anirudh Asuri Mukundan, Thibaut Ménard, Alain Berlemont, Jorge César C Brändle de Motta

To cite this version:

Anirudh Asuri Mukundan, Thibaut Ménard, Alain Berlemont, Jorge César C Brändle de Motta. A comparative study of DNS of airblast atomization using CLSMOF and CLSVOF methods. 29th Annual Conference on Liquid Atomization and Spray Systems (ILASS19), Sep 2019, Paris, France. hal-02318020

HAL Id: hal-02318020

https://hal.science/hal-02318020v1

Submitted on 16 Oct 2019

HAL is a multi-disciplinary open access archive for the deposit and dissemination of scientific research documents, whether they are published or not. The documents may come from teaching and research institutions in France or abroad, or from public or private research centers.

L'archive ouverte pluridisciplinaire **HAL**, est destinée au dépôt et à la diffusion de documents scientifiques de niveau recherche, publiés ou non, émanant des établissements d'enseignement et de recherche français ou étrangers, des laboratoires publics ou privés.

A comparative study of DNS of airblast atomization using CLSMOF and CLSVOF methods

Anirudh Asuri Mukundan*, Thibaut Ménard, Alain Berlemont, Jorge César Brändle de Motta
CNRS UMR6614-CORIA, Rouen, France
*Corresponding author: anirudh.mukundan@coria.fr

Abstract

The results from direct numerical simulations (DNS) of planar pre-filming airblast atomization are presented in this paper. The configuration of the airblast atomization is inspired from a published experimental configuration of Gepperth et al (2012, "Ligament and Droplet Characteristics in Prefilming Airblast Atomization", ICLASS 2012). The simulations have been performed using our in-house Navier-Stokes solver ARCHER. Two DNS have been performed each respectively using coupled level moment of fluid (CLSMOF) and coupled level set volume of fluid (CLSVOF) methods for liquid/gas interface reconstruction. The operating point investigated in the simulations correspond to aircraft altitude relight conditions. The DNS data are post-processed consistent to that of the experimental data to extract droplet and ligament statistics. The droplet diameter distribution from the simulations is found to be having satisfactory agreement with the experimental data. Two breakup mechanisms of atomization are observed: sheet breakup producing small droplets and ligament breakup producing medium and bulgy droplets. The CLSMOF method is observed to produce more medium and bulgy droplets owing to dominant ligament breakup while CLSVOF method produced more number of small droplets owing to predominant sheet breakup mechanism. A good agreement was found between simulations and experiments for Sauter Mean Diameter (SMD) of the droplets. The droplet diameter distribution from the simulations are found to under-predict the peak of the distribution but displays similar profile as that of the experiments. The droplet velocity distribution from the simulations is found to agree well with that of the experiments. The liquid ligaments formed at the trailing edge of the pre-filmer plate are characterized by their lengths. The breakup length of the ligaments, defined as arithmetic mean of the ligament lengths, computed from the simulations agree satisfactorily with the value computed from the experimental data.

Keywords

CLSMOF, CLSVOF, airblast, atomization, drop size distribution, altitude relight

Introduction

With the growing number of short-haul flights, the air traffic is increasing and with that comes the emission regulations norms. Over the past decade, these norms are becoming more stringent. In order to meet these pollution regulations, lean combustion strategies are often employed in aircraft engines. In such strategies, the high mixing between fuel and oxidizer is a primary prerequisite for efficient and cleaner combustion. To that end, often planar pre-filming airblast atomizers are employed for injecting fuel. In planar pre-filming airblast atomization, high speed oxidizer shears off the liquid fuel film injected on a flat plate causing fine breakup leading to production of small to medium sized droplets. The smaller the size of the droplets, the faster is their evaporation and mixing with oxidizer, and thus, more efficient and cleaner is their combustion. Thus, atomization of liquid fuel into droplets has a major impact on the final amount of pollutant emissions. Hence, it is imperative to study this process in order to get better control of it.

The concept of airblast atomization was introduced by Lefebvre and Miller [1]. Since then, there has been multiple experimental studies [2–6] investigating the droplet size distributions far downstream of the injector nozzle. Multiple numerical studies were carried out in simulating cylindrical [7] and planar pre-filming [8–10] airblast atomization. For example, Fuster et al. [11] studied the primary breakup of planar coflowing sheets of water and air at dynamic pressure ratios of 0.5 to 32; Bilger and Stewart Cant [12] focused on the airblast atomization and regime classification for different gas and liquid phase velocities. They classified the different breakup mechanisms into regimes based on the velocity of the gas and liquid fuel. This work used laminar velocity profile for the phases, thus might not necessarily represent the real time fuel injection scenarios. Recently, accurate near field data from the experiments have been extracted by Gepperth et al [5]. In their work, the information about the ligament length, velocity, and breakup frequency were identified. Following their work, Warncke et al [13] presented a combined experimental and numerical study using embedded direct numerical simulations (eDNS) approach of Sauer [14] with classical volume of fluid (VOF) interface capturing technique using OpenFoam. Although a good agreement between experiments and simulations had been observed in their work, the results displayed the limitation of the diffused interface capturing methods used in their simulations.

Thus, to this end, we have used a DNS approach to simulate the planar pre-filming airblast atomization for the same operating point and configuration as described by Warncke et al [13] and compared the results with the experimental work of Gepperth et al [5]. In contrast to Warncke et al [13], we have used full DNS approach and we have employed *sharp interface capturing* methods for accurately capturing the liquid/gas interface within the context of incompressible multiphase flows. In fact, we have performed two DNS each with sharp interface capturing method respectively: coupled level set moment of fluid (CLSMOF) method [15, 16] and coupled level set volume of fluid (CLSVOF) method [17].

This work is licensed under a Creative Commons 4.0 International License (CC BY-NC-ND 4.0).

This paper is organized as follows: first, the equations governing the incompressible multiphase flow solved in our in-house code ARCHER [17–19] are presented followed by presentation of the numerical method of CLSMOF method. The case setup, configuration, and the operating conditions for the DNS are then presented followed by the results from the simulations. In this section, we compare the results from the simulations using CLSMOF and CLSVOF methods and compared each with that of the experimental data. Finally, concluding remarks are drawn upon based on the presented results.

Governing Equations

The solver used in this study is ARCHER, whose capabilities are described extensively in multiple works [17–19]. This solver is structured, parallel, and developed for direct numerical simulations (DNS) of complex and turbulent multiphase flows with the application to study primary breakup of liquid fuel jet. A staggered variable configuration for scalar and vector quantities is used with central finite difference scheme for least numerical dissipation.

The pressure and velocity fields describing the flow are obtained by solving the incompressible Navier–Stokes equations. The following conservative form of the Navier–Stokes equations are solved in ARCHER:

$$\boldsymbol{\nabla} \cdot \boldsymbol{u} = 0, \tag{1}$$

$$\frac{\partial \rho \boldsymbol{u}}{\partial t} + \boldsymbol{\nabla} \cdot (\rho \boldsymbol{u}\, \boldsymbol{u}) = -\boldsymbol{\nabla} P + \boldsymbol{\nabla} \cdot (2\mu \boldsymbol{D}) + \boldsymbol{B}, \tag{2}$$

where $\boldsymbol{u}$ is the velocity field, P is the pressure field, μ is dynamic viscosity, ρ is density, $\boldsymbol{D}$ is the strain rate tensor given as $\boldsymbol{D} = \frac{1}{2}(\boldsymbol{\nabla u} + (\boldsymbol{\nabla u})^T)$, and $\boldsymbol{B}$ is the sum of the body force ($\boldsymbol{B}_{\mathrm{b}}$) and surface tension forces ($\boldsymbol{B}_{\mathrm{st}}$). The force due to surface tension is given as $\boldsymbol{B}_{\mathrm{st}} = \sigma \kappa \delta_I \boldsymbol{n}$ where σ represent the surface tension coefficient, κ is the curvature of the interface computed using the level set signed distance function ϕ as

$$\kappa = -\nabla \cdot \left(\frac{\nabla \phi}{\|\nabla \phi\|_2} \right), \tag{3}$$

and δ_I is the Dirac delta function centered on it. A consistent mass and momentum flux computation [19] is employed. The level set signed distance function ϕ takes positive values for grid points inside liquid phase and negative for grid points inside gas phase in a numerical simulation domain.

A projection method as described in Ménard et al [17] is employed for solving Equations (1) and (2). A 2nd order central difference scheme is employed for discretization of the spatial derivatives to avoid any dissipation. However, the convection term is discretized using 5th order WENO scheme to ensure a robust behavior of the solution. A consistent mass and momentum flux computation [19] is employed. The viscous term is discretized following the method described by Sussman et al [20]. Ghost Fluid Method (GFM) [21] is employed for the spatial discretization of the Poisson equation for taking into account the force due to surface tension as a pressure jump. The resulting linear system of symmetric and positive definite matrix with five diagonals is solved using multigrid algorithm for preconditioning a conjugate gradient (CG) method [18]. The temporal derivatives in this study are discretized using one-step forward Euler scheme.

Numerical Method

In this section, we first briefly summarize the coupled level moment of fluid (CLSMOF) method employed for liquid/gas interface capturing within the context of multiphase flows. Then the numerics behind the CLSMOF interface reconstruction and advection are presented. Finally, a criteria for distinguishing resolved and under-resolved interface is presented.

CLSMOF Method

Within the context of multiphase flows, it is imperative to accurately capture the liquid/gas interfaces. To this end, we have used CLSMOF interface reconstruction method. We have developed in our solver this method as a combination of conventional moment of fluid (MOF) [15, 16, 22, 23] and coupled level set moment of fluid (CLSVOF) [17] methods. This way, it is possible to combine the advantages of both methods: accurate capture of under-resolved liquid droplets from MOF and sharp interface representation from LS methods. The objective is to use a computationally more expensive MOF method only for reconstructing under-resolved liquid structures.

MOF method is a superset of conventional volume of fluid (VOF) method. MOF method tracks both liquid volume fraction (zeroth moment of liquid volume) and phase centroids (first moment of liquid volume) in each mixed computational cell (cell with non-zero liquid volume fraction) in order to numerically reconstruct the interface. A piecewise linear interface calculation (PLIC) method is used for reconstructing the interface. Thus, the equation of the reconstructed interface plane (line in 2D) is given as $ax + by + cz + d = 0$ where interface normal $\boldsymbol{n} = [a, b, c]^T$. The reconstruction of original/reference interface means determining the components of interface normal $\boldsymbol{n}$ and shortest distance of interface from cell center d. In MOF method, we find these two quantities by satisfying volume conservation (Equation (4)) and least centroid defect (Equation (5)). The centroid defect is defined as the distance between the phase centroids of the reference and actual/reconstructed interface. The two conditions are:

$$\mid F^{\mathrm{ref}} - F^{\mathrm{act}}(\boldsymbol{n}, d) \mid = 0, \text{ and} \tag{4}$$

$$E^{\mathrm{MOF}}(\boldsymbol{n}, d) = \min_{\text{Eq. (4) holds}} \left\| \boldsymbol{x}^{\mathrm{ref}}_{\mathrm{COM}} - \boldsymbol{x}^{\mathrm{act}}_{\mathrm{COM}}(\boldsymbol{n}, d) \right\|_2 . \tag{5}$$

This work is licensed under a Creative Commons 4.0 International License (CC BY-NC-ND 4.0).

where F represent liquid volume fraction and $\boldsymbol{x}_{\mathrm{COM}}$ is the liquid phase centroid. All the variables containing the superscript "ref" represents the variables pertaining to the original (reference) interface while those containing the superscript "act" represents the variables pertaining to the reconstructed (actual) interface. The reference interface is chosen for a fluid (either liquid/gas) based on the farthest distance of its centroid from the cell center x_{C_Ω} (where C_Ω is a computational cell inside the domain Ω), i.e.,

$$\text{Reference fluid} = \begin{cases} \text{liquid}, & \left\|\boldsymbol{x}^{\mathrm{ref}}_{\mathrm{COM,liq}} - \boldsymbol{x}_{C_\Omega}\right\| > \left\|\boldsymbol{x}^{\mathrm{ref}}_{\mathrm{COM,gas}} - \boldsymbol{x}_{C_\Omega}\right\| \\ \text{gas}, & \text{otherwise.} \end{cases} \tag{6}$$

Thus, the centroid defect is minimized for the phase with the least volume in the cell. The rationale behind this approach is that, the interface orientation has highest sensitivity to the centroid defect of the phase with least volume. For the purpose of illustration, Figure 1 shows a typical computational cell in 2D with the reference and reconstructed interfaces based on liquid as reference fluid. The parameter d is computed as a result of satisfying the volume

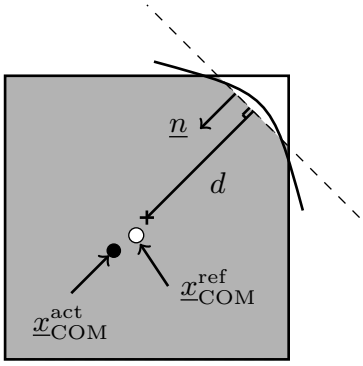

Figure 1. Computational cell with reference (solid line) and reconstructed (dashed line) interfaces and liquid centroid.

conservation condition (Equation (4)) upto the machine precision using Newton-Raphson method. The interface normal $\boldsymbol{n}$ is obtained from minimizing the centroid defect E^{MOF} using Gauss-Newton minimization algorithm. It is to be mentioned that this algorithm finds local minima and not global minima. The reference liquid volume fraction F is advected by a directionally split algorithm described in [24] and the reference liquid and gas phase centroids are advected using a directionally split Eulerian Implicit-Lagrangian Explicit (EI-LE) scheme. For more details, the readers are referred to Asuri Mukundan et al [15, 16].

The coupled level set volume of fluid (CLSVOF) method of Ménard et al [17] is used for obtaining the level set function for interface capturing in our solver.

Interface Resolution Quality (IRQ)

The main idea of the CLSMOF method development is to use MOF only when it is necessary. This necessity is driven by presence of under-resolved liquid structures which are smaller in size than the employed mesh resolution. Thus, it is required to find and distinguish resolved and under-resolved liquid structures from one another. To this end, we propose a criteria called *interface resolution quality* (IRQ) which is expressed as

$$\mathrm{IRQ} = \frac{1}{\Delta x \mid \kappa \mid}, \tag{7}$$

where Δx is the mesh spacing and κ is the liquid/gas interface curvature. The threshold value of IRQ determines which of the liquid structures in the domain are resolved and which are under-resolved. Based on the literature [25, 26], we decided to use the threshold value of 2.0 for IRQ. This means, for any computational cell containing a liquid phase and has a value of IRQ less than 2.0 (correspondingly, less than 8 cells along the liquid structure effective spherical diameter) would be treated as under-resolved liquid cell structure, thus, MOF will be employed for interface reconstruction. For all other IRQ values, the level set function from CLSVOF method will be used for interface reconstruction. It is to be remarked that Jemison et al [23] used a similar criteria with a higher threshold value in their work.

Case Setup

A planar pre-filming airblast atomizer configuration is considered in this work. Figure 2a represents a geometry simplification of the annular atomizer used in our Direct numerical simulations (DNS). This simplified geometry is inspired from the work of Gepperth et al [5] and Warncke et al [13].

Operating Conditions

Fuel injection in aircraft engines are characterized by high Reynolds and Weber number. A detailed investigation of fuel injection in such highly turbulent environment is challenging using DNS. A moderate operating point is thus chosen with a comparatively low Reynolds and liquid film Weber number. This operating point correspond to

This work is licensed under a Creative Commons 4.0 International License (CC BY-NC-ND 4.0).

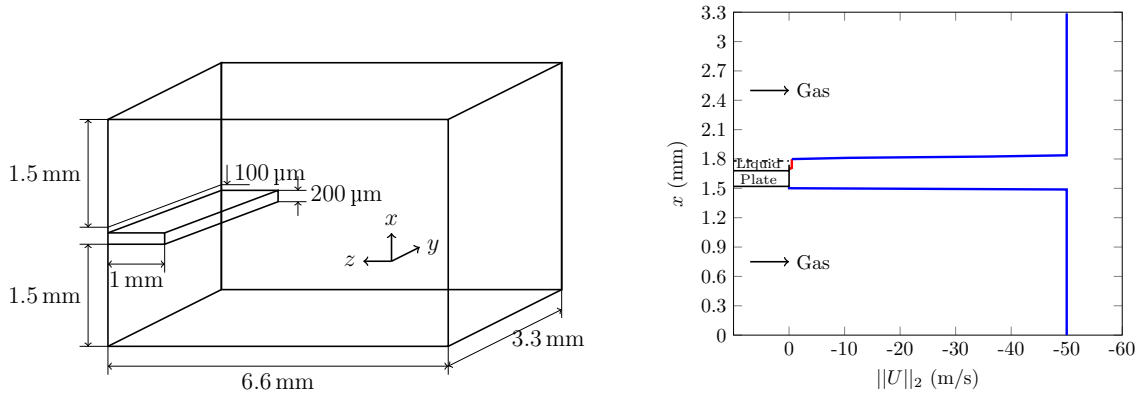

(a) DNS computational domain

(b) Velocity profile for liquid and gas phases

Figure 2. DNS Domain (a) and inflow phase velocity profile (b): liquid phase (——); gas phase (——). Negative velocity is due to downstream direction oriented along negative $z-$direction.

the aircraft altitude relight conditions [27] and allows an adequate resolution of the atomization events. The operating conditions are summarized in Table 1 The liquid fuel used in this study correspond to Shellsol D70 with a low surface tension at ambient conditions. The channel half width $H_{\mathrm{chw}} = 4\,\mathrm{mm}$ and liquid film thickness $h_{\mathrm{l}} = 100\,\mu\mathrm{m}$. The non-dimensional numbers such as gas phase Reynolds number ($\mathrm{Re_g}$), liquid film Weber number ($\mathrm{We_l}$), and momentum flux ratio (M) are defined within this work as

$$\mathrm{Re_g} = \frac{\overline{u}_{\mathrm{g}} H_{\mathrm{chw}}}{\nu_{\mathrm{g}}}, \tag{8}$$

$$\mathrm{We_l} = \frac{\rho_{\mathrm{g}}(\overline{u}_{\mathrm{g}} - \overline{u}_{\mathrm{l}})^2 h_{\mathrm{l}}}{\sigma}, \quad \text{and} \tag{9}$$

$$M = \frac{\rho_{\mathrm{g}} \overline{u}_{\mathrm{g}}^2}{\rho_{\mathrm{l}} \overline{u}_{\mathrm{l}}^2}. \tag{10}$$

Table 1. Operating Conditions Summary

Liquid properties	$\overline{u}_{\mathrm{l}} = 0.5\,\mathrm{m/s}$	$\rho_{\mathrm{l}} = 770\,\mathrm{kg/m^3}$	$\nu_{\mathrm{l}} = 2.0 \times 10^{-6}\,\mathrm{m^2/s}$
	$\sigma = 0.0275\,\mathrm{kg/s^2}$		
Gas properties	$\overline{u}_{\mathrm{g}} = 50\,\mathrm{m/s}$	$\rho_{\mathrm{g}} = 1.2\,\mathrm{kg/m^3}$	$\nu_{\mathrm{g}} = 1.5 \times 10^{-5}\,\mathrm{m^2/s}$
Non-dimensional numbers	$\mathrm{Re_g} = 13\,333$	$\mathrm{We_l} = 10.69$	$M = 15.58$

Computational Setup

The air flow inlet is located each above and below the pre-filmer plate. A flat velocity profile with the magnitude of the mean liquid and gas phase velocity is imposed as the inlet velocity profile as shown in Figure 2b. The DNS domain has been chosen in such a way that there is enough length along the downstream direction to analyze atomization but also kept as small as possible to avoid blow up of the computational cost.

The faces of the pre-filmer plate are treated as walls using the staircase immersed boundary method (SIBM). In this method, the shape of the pre-filmer plate is approximated such that it fits in the Cartesian grid lines. Thus, fluxes over the cell faces containing the solid pre-filmer plate can be computed like that for a no-slip boundary cell face. An injection boundary condition has been used on the gas and liquid fuel injection boundary plane, periodic boundary condition on the transverse $y-$direction, and outflow boundary conditions on the rest of the boundaries. Turbulence in the liquid fuel is initiated using the method of synthetic turbulence of Klein et al [28].

A computational mesh with a constant mesh spacing of $\Delta x = \Delta y = \Delta z = 12.89\,\mu\mathrm{m}$ has been employed throughout the domain resulting in a total of 33.5 million cells. For the value of Reynolds number employed in this study, the Kolmogorov length scale was found to be $\eta = 12\,\mu\mathrm{m}$. Thus, based on [29], the required minimum grid spacing is $\Delta x_{\mathrm{min}} \approx 25\,\mu\mathrm{m}$. With the grid resolution used in this work, it can be said that we will be able to resolve the predominant scales of motion. The simulation has been run on 1024 processors in CRIANN supercomputing facility.

Experimental Comparison

In order to validate the results from DNS, we will be comparing with the experimental data from the work done at the Institut für Thermische Strömungsmaschinen (ITS) at Karlsruhe Institut für Technologie. The experiments have been performed for 30 s of physical time and double frame images (in both $y-z$ and $x-z$ plane views) that are phase

This work is licensed under a Creative Commons 4.0 International License (CC BY-NC-ND 4.0).

shifted by 10 µs. Each droplet in the double image was considered for the computation of statistics. To statistically derive robust results for the ligament and droplet sizes, an efficient algorithm based on the particle and ligament tracking velocimetry developed by Müller [30] with an extension to Depth of Field (DoF) correction to increase the measurement accuracy was used. For more details on the measurement and post-processing techniques employed in the experimental work, the reader is referred to [5, 13].

Results and Discussion

Post-processing Techniques

The post-processing and analysis of the DNS data is split into two parts: analysis of droplets and analysis of accumulated liquid ligaments at the trailing edge of the pre-filmer plate.

In order to determine the probability distribution of the droplets in the domain, a connected component labelling (CCL) algorithm is used. This algorithm finds list of all the liquid structures in the domain at a given time instant by using a 8-cell neighbor connectivity search for liquid presence. This list contains all the attributes of the liquid structures such as velocity components, surface area, diameter, and volume. It is to be remarked that the liquid droplet structure diameter is derived from its volume with the assumption that liquid structure is spherical.

The extraction of results for the liquid ligaments accumulated at the trailing edge of the pre-filmer plate such as ligament lengths and breakup length is challenging. To this end, we have used an algorithm that is split into four steps. First, the 3D DNS data (c.f. Figure 3a) is reduced to a 2D data analogous to the shadowgraphy images by assigning label value of 0 (for gas) and 1 (for liquid) to each cell with zero and non-zero liquid volume fraction respectively. Second, these label values are summed up along cross-stream $x-$direction to generate a projected top view ($y - z$ plane view) (c.f. Figure 3b). Any cell in this top view with a summed label value greater than 1 indicates presence of liquid in this view. Third, a CCL algorithm is applied for these summed up label values to identify the biggest liquid structure, i.e., the accumulated liquid at the trailing edge of pre-filmer plate (c.f. Figure 3c). Finally, the 1D interface contour is identified using the method described in [31,32] that characterizes the interface of this accumulated liquid (c.f. Figure 3d). This procedure has been applied to every time step since the first breakup event has occurred.

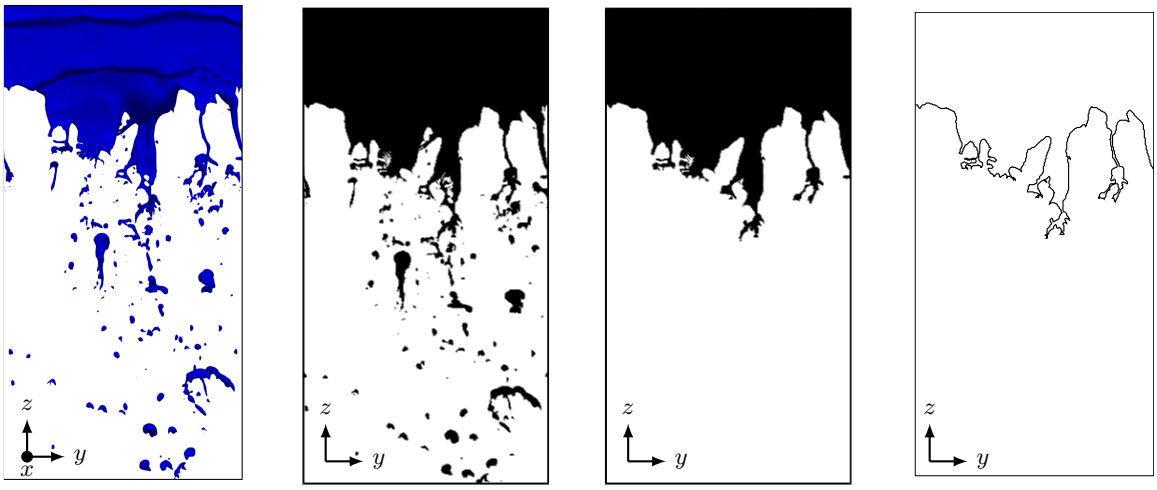

(a) 3D DNS data (b) 2D Projected DNS data (c) Biggest liquid structure (d) 1D phase interface

Figure 3. Reduction of 3D to 1D data for computing ligament characteristics for $t = 5.05$ ms.

Droplet characterization

We now present the quantitative results regarding the liquid droplets. They are characterized using diameter and streamwise velocity distributions. The liquid droplet structures are detected throughout the DNS domain for each sampling time step. The sampling is done every 1000 flow solver iterations. In order to have single count of a liquid packet/droplet, we developed an algorithm that compares the position of each droplet between adjacent sampling time steps (t^n and t^{n+1}, for example) and adds to the list of droplets for distribution plot only when it goes out of the domain at t^{n+1}. The smallest droplet diameter measured from the experiments is 15 µm, while that from CLSMOF simulations is 9.73 µm and from CLSVOF simulations is 20 µm which are approximately $0.75\Delta x$ and $1.55\Delta x$ respectively. Figure 4 shows the plot of the probability density function of the droplet diameter and the droplet streamwise velocity. The data presented in these plots from the simulations are not clipped to the smallest droplet diameter measured from the experiments. This way, we can display and compare the accuracy of the CLSVOF and CLSMOF methods against the experimental capability. From this figure, it can be seen that CLSVOF method is producing smaller droplets than the CLSMOF method. This could be attributed to the numerical surface tension that the CLSMOF method is introducing to the interface. Since CLSMOF method uses the volume fraction data from the corresponding cell to compute the interface unit normal (as opposed to using neighboring cell data such as in CLSVOF), there arises a modification to the interface curvature in that cell. Such a modification

This work is licensed under a Creative Commons 4.0 International License (CC BY-NC-ND 4.0).

often leads to a change in the surface tension generated on the interface in comparison to the expected surface tension. This change is called numerical surface tension within this work. Moreover, the profile of the curve for the CLSMOF method is similar to that of the experiments. Furthermore, more medium sized droplets are produced in the simulations when CLSMOF method is used. Droplet diameters upto 300 µm are found from the simulations.

Owing to the quasi-bimodal distribution of the drop diameter quantity, two independent breakup mechanisms are responsible for droplet formation. First, the sheet breakup wherein a thin sheet of liquid is formed because of the shearing of the liquid by the gas developing holes in them thereby producing droplets whose size are comparable to that of the thickness of the sheet. Since the liquid sheet is often few computational cells thick, this breakup mechanism produces small droplets attributing to the peak near 35.5 µm. The second breakup mechanism is due to the breakup of liquid ligaments. The liquid fuel gets accumulated at the trailing edge of the pre-filmer plate, due to the high speed flow of gas over it, forming thin long irregular shaped ligaments. These ligaments then breakup into droplets due to Rayleigh-Plateau instability. Such breakup often produces medium and bulgy droplets attributed to the peak near 70 µm in the plot of the droplet size distribution. Thus, from this information, we can infer that CLSMOF is producing medium sized droplets owing to the predominant occurrence of ligament breakup mechanism. Moreover, as shown by Asuri Mukundan et al [15,16], the CLSMOF method is able to capture the small under-resolved droplets that are one-order smaller than the employed mesh resolution. This can be seen from the small peak near the very small droplets diameter in the plot corresponding to droplet diameters that are one order smaller than the employed mesh spacing. Finally, the Sauter Mean Diameter (SMD) computed from the DNS for CLSMOF method is 130.13 µm and CLSVOF method is 103.68 µm while that is computed from the experimental data is 154.8 µm. Although there is a slight under-prediction from the simulations, this discrepancy could be attributed to the long measurement time and more number of droplets detected in the experiments than in the simulations. Nevertheless, the values from simulations are of the same order as that of the experiments. Moreover, the SMD from DNS using CLSMOF method is in very good agreement with that from the experiments.

With regards to the droplet velocity distribution, the global inference is that the simulation over-predicts the peak of the results. On one hand, the results from the CLSMOF method has peak at 12.4 m/s while that from CLSVOF is at 16 m/s in comparison to 13.5 m/s from the experiments. A more realistic inflow velocity profile for the phases in the DNS could help in matching with the experiments.

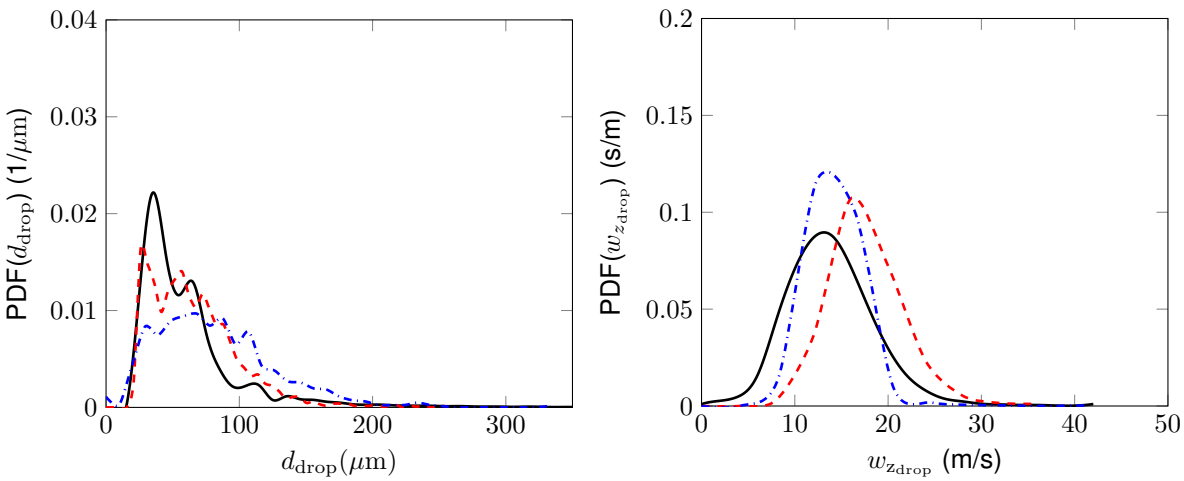

(a) Droplet size distribution

(b) Droplet velocity distribution

Figure 4. Characterization of droplets: Experiments (——), CLSVOF (- - -), and CLSMOF (-·-·-).

Ligament characterization

Now, we present the characterization of liquid ligaments formed at the trailing edge of the pre-filmer plate. Due to the high velocity of the gas, the liquid fuel gets accumulated at the trailing edge of the pre-filmer plate. Due to the high difference between the velocity of liquid fuel and air, this accumulated liquid is stretched downstream into thin, long, and irregular shaped ligaments. These ligaments are characterized in our study based on their lengths l_{lig} and the global breakup length l_{breakup} quantities. The latter is computed as the arithmetic mean of all the individual ligament lengths over all sampled time steps.

In order to obtain the individual ligament lengths, we post-processed the DNS data from both the simulations, the details of which are presented as follows. Referring Figure 5, we have defined a single ligament length l_{lig} as the distance between the ligament peak and the trailing edge of the pre-filmer. To compute the ligament length for a single time step, the 1D phase interface contour (c.f. Figure 3) is used. The maximum dips in this 1D phase interface (blue squares) shown in Figure 5b along the downstream direction is used for identifying the ligaments. The critical point in this identification is to compute the true ligament length by eliminating the effect of the wrinkling in the interface. For this reason, following [13], we use a criterium of 50 µm distance between the adjacent minima and maxima (measured along the streamwise $z-$direction) as a threshold to eliminate this effect and obtain a more

This work is licensed under a Creative Commons 4.0 International License (CC BY-NC-ND 4.0).

global behavior. The true maxima (maxima obtained after applying the the criterium) in the interface are shown in Figure 5c with the squares indicating the location of the maximum dip in the interface in the downstream direction. The length of these resulting maximum dips (called true ligament lengths hereon) are computed from the edge of the pre-filmer plate. The breakup length l_{breakup} is then computed as the arithmetic mean of these true ligament lengths over all time steps. The post-processing used for the experimental data is presented by Warncke et al [13].

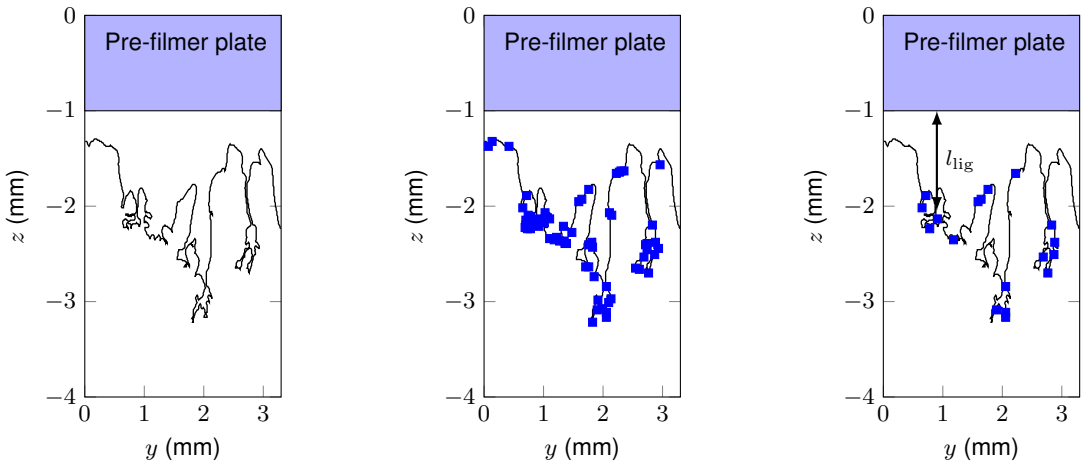

(a) 1D interface contour (b) All identified maxima (c) True maxima after 50 µm criterium

Figure 5. Detection of phase interface peak (blue squares) for ligament length computation.

From this post-processing procedure, the breakup lengths for the simulations using CLSMOF method is computed to be $l_{\mathrm{breakup}} = 1.6\,\mathrm{mm}$ while that using CLSVOF is $l_{\mathrm{breakup}} = 1.17\,\mathrm{mm}$. The experimental value measures 3.2 mm. The breakup length from the simulations are smaller in magnitude albeit of the same order as that of the experimental value. Per the study of Sauer et al [33], when the breakup length is computed as the maximum of all the ligament lengths, the result from our simulation is 3.74 mm which is only a little over-prediction in comparison to the experiments. A small amount of ligaments with lengths longer than the length of streamwise direction of the DNS domain were observed in the experiments that resulted in greater breakup lengths in experimental data. Furthermore, a total of 12 201 and 1657 ligaments have been identified respectively for DNS using CLSMOF and CLSVOF methods while 13 000 ligaments from the experiments. This difference in the total number of ligaments of one order of magnitude between the two methods could stem from multiple factors such as CLSMOF method could be introducing numerical surface tension in the flow when reconstructing the liquid/gas interface, the wrinkling effect of the interface is not fully removed when identifying the ligaments. This could mean that the 50 µm criterium would have to be changed.

Another perspective on the ligament characterization can be obtained from the frequency distribution of their lengths. This is shown in Figure 6. From this figure, we can infer that the frequency distribution is shifted towards smaller ligament lengths in the simulations. This could be due to three factors and reasons: first, no ligaments measured from our simulations reaches the outlet of the domain; second, there was greater time period for the sampling in the experiments, and therefore, a higher amount of samples compared to the simulations; and third, the field of view of measurement for experiments are larger than that of the DNS, thus, longer ligament lengths that are greater than the length of the streamwise direction of the DNS domain are observed. Furthermore, these under-predictions could be attributed to the insufficiency of the mesh resolution to capture the breakup events.

Conclusions

In this paper, we have presented results from direct numerical simulations (DNS) of planar pre-filming airblast atomization performed using coupled level set moment of fluid (CLSMOF) method and coupled level set volume of fluid (CLSVOF) method. The CLSMOF method is a hybrid between classical moment of fluid (MOF) and CLSVOF methods. The MOF method uses both phase volume fraction and phase centroids in reconstructing the liquid/gas interface. This method does not require phase volume data from neighbor cells thereby leading to uniform treatment of interior and boundary cells as well as resolution of the interface to be as high as the employed mesh resolution. Within the concept of CLSMOF method, the classical MOF method is used only for reconstructing the under-resolved liquid structures. Such structures are identified using interface resolution quality criterium.

The DNS have been performed for aircraft altitude relight operating conditions using Shellsol D70 that is comparable to jet A-1 fuel used in aircraft engines. Quantitative results presented in this work have been classified into droplet and ligament characterizations. The droplets have been characterized through diameter and velocity probability distributions. We have identified two mechanisms of breakup: sheet and ligament breakup mechanisms. We have observed that CLSMOF method produces medium and bulgy droplets due to predominant ligament breakup while the CLSVOF method produces large number of small droplets due to predominance of sheet breakup mechanism. A good agreement has been achieved for the Sauter Mean Diameter between the DNS and experiments. The agreement between simulations and experiments have been found to be satisfactory for the droplet diame-

This work is licensed under a Creative Commons 4.0 International License (CC BY-NC-ND 4.0).

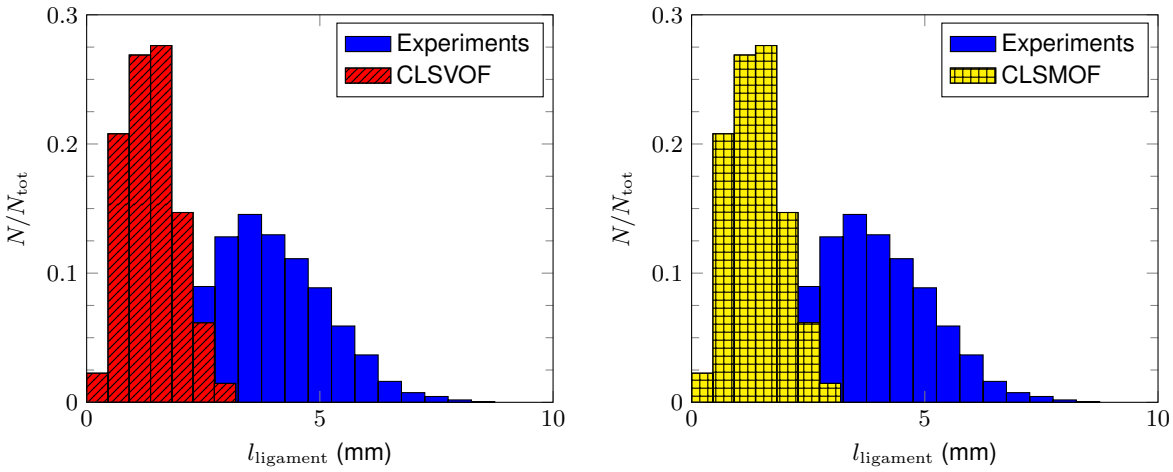

(a) CLSVOF method

(b) CLSMOF method

Figure 6. Frequency distribution of ligament length.

ter distribution. The velocity distributions from the simulations using CLSMOF and CLSVOF methods have been demonstrating good agreement with the experiments. The liquid ligaments at the trailing edge of the pre-filmer plate have been characterized by their length. The breakup length computed as the arithmetic mean of all ligament lengths is found to be of the same order as that of experimental data. The frequency distributions of the ligament lengths found that the simulations under-predict the ligament lengths.

In future, three advancement to the current study have been considered: first, employment of finer mesh resolution in the DNS; second, using a realistic inflow velocity profile for phases such as fully developed turbulent channel flow profile that closely represent the fuel injection conditions in aircraft engines, and third, increasing the size of the numerical domain and simualting for long time period of fuel injection.

Acknowledgements

The funding for this project from the European Union's Horizon 2020 research and innovation programme under the Marie Skłodowska-Curie grant agreement N° 675676 is gratefully acknowledged. The computing time at CRIANN (Centre Régional Informatique et d'Applications Numériques de Normandie) under the scientific project No. 2003008 and at GENCI-[TGCC/CINES/IDRIS] (Grant2019-2613) are also gratefully acknowledged. The authors would like to thank Prof. Dr. Jean-Bernard Blaisot for graciously sharing his algorithm of finding the 1D interface contour. The authors wish to thank Prof. Rainer Koch and his group at Institut für Thermische Strömungsmaschinen in Karlsruher Institut für Technologie (KIT), Germany for graciously sharing their experimental data.

References

[1] Lefebvre, A. H. and Miller, D. The development of an air blast atomizer for gas turbine application. Technical Report AERO No. 193, The College of Aeronautics Cranfield (1966).
[2] Lasheras, J. C., Villermaux, E., and Hopfinger, E. J. *Journal of Fluid Mechanics* 357:351–379 (1998).
[3] Bhayaraju, U. C. and Hassa, C. *Atomization and Sprays* 19(12):1147–1169 (2009).
[4] Jasuja, A. K. In Proceedings of the 10th ICLASS, 27th August–1st September, Kyoto, Japan (2006).
[5] Gepperth, S., Müller, A., Koch, R., and Bauer, H.-J. In Proceedings of the ICLASS 2012, 12th Triennial International Conference on Liquid Atomization and Spray Systems, Heidelberg, Germany, September 2-6, 2012 (2012).
[6] Holz, S., Chaussonnet, G., Gepperth, S., Koch, R., and Bauer, H.-J. In ILASS – Europe 2016, 27th Annual Conference on Liquid Atomization and Spray Systems, 4-7 September 2016, Brighton, UK (2016).
[7] Chiodi, R. and Desjardins, O. In 55th AIAA Aerospace Sciences Meeting (2017).
[8] Chaussonnet, G., Riber, E., Vermorel, O., Cuenot, B., Gepperth, S., and Koch, R. In ILASS-Europe 2013, 25th European Conference on Liquid Atomization and Spray Systems, Chania, Greece, 1-4 September (2013).
[9] Agbaglah, G., Chiodi, R., and Desjardins, O. *Journal of Fluid Mechanics* 812:1024–1038 (2017).
[10] Braun, S., Weith, L., Holz, S., Dauch, T. F., Keller, M. C., Chaussonnet, G., Gepperth, S., Koch, R., and Bauer, H.-J. *International Journal of Multiphase Flow* (2019 (in press accepted manuscript)).
[11] Fuster, D., Matas, J.-P., Marty, S., Popinet, S., Hoepffner, J., Cartellier, A., and Zaleski, S. *Journal of Fluid Mechanics* 736:150–176 (2013).
[12] Bilger, C. and Stewart Cant, R. *Atomization and Sprays* 28(1):65–89 (2018).
[13] Warncke, K., Gepperth, S., Sauer, B., Sadiki, A., Janicka, J., Koch, R., and Bauer, H.-J. *International Journal of Multiphase Flow* 91:208–224 (2017).
[14] Sauer, B., Sadiki, A., and Janicka, J. *The Journal of Computational Multiphase Flows* 6(3):179–192 (2014).
[15] Asuri Mukundan, A., Ménard, T., Berlemont, A., and Brändle de Motta, J. C. In 10th International Conference on Computational Fluid Dynamics ICCFD10 2018, 9–13 July, Barcelona, Spain (2018).

This work is licensed under a Creative Commons 4.0 International License (CC BY-NC-ND 4.0).

[16] Asuri Mukundan, A., Ménard, T., Berlemont, A., and Brändle de Motta, J. C. In Proceedings of the 14th ICLASS, July 22nd-26th, Chicago, USA (2018).
[17] Ménard, T., Tanguy, S., and Berlemont, A. *International Journal of Multiphase Flow* 33(5):510–524 (2007).
[18] Tanguy, S. and Berlemont, A. *International Journal of Multiphase Flow* 31:1015–1035 (2005).
[19] Vaudor, G., Ménard, T., Aniszewski, W., Doring, M., and Berlemont, A. *Computers & Fluids* 152:204–216 (2017).
[20] Sussman, M., Smith, K. M., Hussaini, M. Y., Ohta, M., and Zhi-Wei, R. *Journal of Computational Physics* 221(2):469–505 (2007).
[21] Fedkiw, R., Aslam, T., Merriman, B., and Osher, S. *Journal of Computational Physics* 152(2):457–492 (1999).
[22] Dyadechko, V. and Shashkov, M. *Journal of Computational Physics* 227:5361–5384 (2008).
[23] Jemison, M., Loch, E., Sussman, M., Shashkov, M., Arienti, M., Ohta, M., and Wang, Y. *Journal of Scientific Computing* 54:454–491 (2013).
[24] Weymouth, G. D. and Yue, D. K.-P. *Journal of Computational Physics* 229(8):2853–2865 (2010).
[25] Gorokhovski, M. and Herrmann, M. *Annual Review of Fluid Mechanics* 40:343–366 (2008).
[26] Shinjo, J. and Umemura, A. *International Journal of Multiphase Flow* 36(7):513–532 (2010).
[27] Mosbach, T., Sadanandan, R., Meier, W., and Eggels, R. In Proceedings of the ASME Turbo Expo 2010: Power for Land, Sea, and Air, Volume 2: Combustion, Fuels and Emissions, Parts A and B, Glasgow, UK, June 14–18, 2010, volume 2 (2010).
[28] Klein, M., Sadiki, A., and Janicka, J. *Journal of Computational Physics* 186(2):652–665 (2003).
[29] Pope, S. B. Turbulent Flows. Cambridge University Press (2000).
[30] Müller, A. Experimentelle Untersuchung des Zerstäubungsverhaltens luftgestützter Brennstoffdüsen bei oszillierenden Strömungen. Ph.D. thesis, Institut für Thermische Strömungsmaschinen (ITS), Karlsruhe Institut für Technologie (2015).
[31] Fdida, N. and Blaisot, J.-B. In ISFV13–13th International Symposium on Flow Visualization, FLUVISU12 - 12th French Congress on Visualization in Fluid Mechanics July 1-4, 2008, Nice, France (2008).
[32] Blaisot, J.-B. In 14th ICLASS, July 22-26, Chicago, USA (2018).
[33] Sauer, B., Sadiki, A., and Janicka, J. *Atomization and Sprays* 26(3):187–217 (2016).

This work is licensed under a Creative Commons 4.0 International License (CC BY-NC-ND 4.0).